Journal of Applied Pharmaceutical Research
Volume 13 Issue 6, Year of Publication 2025, Page 47 – 61
DOI: https://doi.org/10.69857/joapr.v13i6.1625

Check for updates

Research Article

JOURNAL OF APPLIED PHARMACEUTICAL RESEARCH | JOAPR
www.japtronline.com ***ISSN: 2348 – 0335***

DEVELOPMENT AND OPTIMIZATION OF ETRASIMOD-LOADED pH-DEPENDENT NANOPARTICLES FOR COLON TARGETED DRUG DELIVERY

Rahul Godge[1]*, Tejas Sahane[1], Shubham Mhaske[1], Sneha Vikhe[1], Santosh Dighe[2]

Article Information
Received: 28th July 2025
Revised: 22nd October 2025
Accepted: 30th November 2025
Published: 25th December 2025

Keywords
Etrasimod, pH-dependent nanoparticles, Colon-targeted delivery, Factorial design, Inflammatory bowel disease, Controlled release.

ABSTRACT

Background: Etrasimod-loaded pH-sensitive nanoparticles offer a promising strategy for targeted drug delivery to the colon, minimizing systemic exposure and enhancing therapeutic efficacy. A Quality-by-Design framework enables systematic optimization of formulation parameters to ensure robust performance and site-specific release. This represents the first systematic development of pH-responsive nanoparticles for etrasimod delivery and the first application of factorial design optimization for S1P receptor modulator nanoformulations. **Methodology:** Etrasimod-loaded pH-dependent nanoparticles were prepared via nanoprecipitation using Eudragit S100 and Eudragit RL100 polymers. The formulation was optimised using a 3^2 full factorial design with polymer concentrations as independent variables. The nanoparticles were characterised by particle size, zeta potential, entrapment efficiency, and drug release. The optimised formulation underwent comprehensive physicochemical characterisation (FTIR, DSC) and 6-month accelerated stability testing. **Results and Discussion:** The optimised formulation (TF5) containing 90% Eudragit S100 and 10% Eudragit RL100 exhibited optimal characteristics with a particle size of 142.6±5.4 nm, zeta potential of -23.5±1.8 mV, and entrapment efficiency of 73.4±3.2%. FTIR and DSC studies confirmed drug-polymer compatibility with minimal interaction. The in vitro release profile demonstrated controlled initial release (9.8% at 1 hour) followed by complete drug liberation (94.2% at 12 hrs) at pH 7.2. The formulation remained stable for 6 months at 40 °C ± 2 °C and 75% ± 5% RH, with minimal changes in critical quality attributes. **Conclusion:** The developed pH-dependent nanoparticulate system offers a promising platform for colon-targeted delivery of etrasimod, demonstrating optimal physicochemical properties, controlled release characteristics, and excellent stability. This formulation approach shows potential to improve therapeutic outcomes in inflammatory bowel disease by enhancing colonic drug delivery.

[1]*Department of Pharmaceutical Quality Assurance, Pravara Rural College of Pharmacy, Pravaranagar, Loni (Bk), Ahmednagar, Maharashtra, India, 413736.*
[2]*Department of Pharmacology, Pravara Rural College of Pharmacy, Pravaranagar, Loni (Bk), Ahmednagar, Maharashtra, India, 413736.*

For Correspondence: **rahulgodge@gmail.com**

INTRODUCTION

There are about 6.8 million individuals worldwide who suffer from inflammatory bowel disease (IBD), which includes Crohn's disease and ulcerative colitis [1]. It is rising at an alarming rate of 7.1% per year [2]. In wealthy nations alone, the cost of direct treatment surpasses $31 billion, and each patient's annual productivity loss is predicted to be $14,000 [3]. The systemic adverse effects, limited colonic targeting, and decreased efficacy during illnesses when intestinal transit accelerates are some of the major drawbacks of current therapy techniques [4]. Traditional formulations exhibit inferior therapeutic effects due to early drug release in the upper gastrointestinal tract and insufficient mucosal retention period [5]. Approximately 30–40% of patients do not respond to the first treatment, and up to 40% of initial responders experience secondary loss of response within a year, despite recent advances in biologic therapies. This underscores the urgent need for new medication delivery methods with targeted colonic release to maximize therapeutic effectiveness and reduce systemic exposure [6]. The chemical structure of Etrasimod is shown in Figure 1, which depicts the molecular architecture of the active compound under investigation to provide structural clarity and to elucidate interactions with biological targets, thereby aiding the interpretation of pharmacodynamic and pharmacokinetic data.

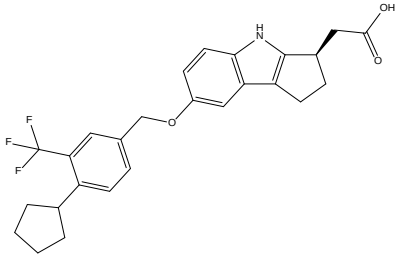

Figure 1: Chemical structure of Etrasimod

With a strong affinity for S1P1, S1P4, and S1P5 receptors, Etrasimod is a selective sphingosine-1-phosphate (S1P) receptor modulator that shows promise in IBD therapy [7]. With its ideal lipophilicity (log P: 3.2) and strong immunomodulating action, it inhibits lymphocyte egress from lymphoid tissues, hence lowering inflammatory cell intrusion into intestinal tissues from this tiny molecule (molecular weight 427.5 g/mol) [8]. In patients with ulcerative colitis, recent phase III clinical trials have shown notable improvements in endoscopic response (43.7% vs 26.5% with placebo; $p<0.001$) and clinical remission rates (26.3% vs 15.2% with placebo; $p<0.001$). Etrasimod's mechanism involves functional antagonism of S1P1 receptors, leading to receptor internalization and degradation and reducing circulating lymphocytes without affecting immune surveillance [9]. Because of its selectivity profile, which largely spares S1P3 receptors implicated in bradycardia, etrasimod exhibits modest cardiac effects, unlike previous-generation S1P modulators. Its oral bioavailability (84%) and moderate plasma half-life (32 hours) make it a perfect choice for modified-release formulations. Oral delivery of etrasimod is challenging owing to variable absorption due to its lipophilicity (log P = 3.2), premature release in the upper gastrointestinal tract, first-pass metabolism, and reduced residence time in inflamed tissue. The developed pH-responsive nanoparticles address these by preventing release below pH 7 (Eudragit S100), enhancing mucosal adhesion through optimized size/charge, protecting against gastric degradation, and sustaining colonic release for 12 hours, thereby maximizing local therapeutic effect while minimizing systemic exposure [10]. Through the unique pH gradient across the gastrointestinal tract, pH-dependent nanoparticle systems offer a novel method for colon-targeted medication delivery [11]. These polymeric nanocarriers include pH-responsive polymers such as Eudragit S100 and L100, which remain intact in the acidic gastric environment (pH 1-3) and dissolve only at colonic pH (>7) [12]. With in vitro studies showing <10% release at gastric pH compared with>85% at colonic pH, this focused approach markedly reduces early drug release [13]. As demonstrated by 2.7-fold higher tissue concentrations than standard formulations, nanoparticles further improve therapeutic efficacy by increasing mucosal adherence, longer retention time, and enhanced cellular absorption. Precision in particle size (100–200 nm), surface charge, and drug encapsulation efficiency (>80%) is enabled by advanced production methods, including ionotropic gelation and nanoprecipitation. Furthermore, these solutions address a major limitation of conventional formulations, which generally undergo early degradation in IBD-affected tissues, by demonstrating greater stability in inflammatory microenvironments characterized by elevated enzyme activity and oxidative stress [14]. This study aims to develop and optimise etrasimod-loaded pH-dependent nanoparticles for targeted colonic drug delivery in the treatment of IBD. We specifically aim to study polymer ratios that affect pH-dependent release kinetics and define nanoparticle stability under accelerated conditions.

MATERIALS AND METHODS

Materials

Etrasimod (analytical grade, purity ≥99.5%, MW 427.5 g/mol) was obtained as a gift sample from MSN Laboratories

(Hyderabad, India). Eudragit S100 (methacrylic acid-methyl methacrylate copolymer, MW ~125,000 Da) and Eudragit RL100 (methyl methacrylate-co-ethyl acrylate polymer, MW ~150,000 Da) were procured from Sciquaint Chemicals, Pune, India. Poloxamer 188 (Pluronic F68, MW ~8,400 Da), Potassium dihydrogen phosphate (analytical grade, purity ≥99.0%), and sodium hydroxide (analytical grade, purity ≥98.0%) were obtained from Neeta Chemicals (Pune, India). Acetone (HPLC grade, ≥99.9% purity) and ethanol (HPLC grade, ≥99.9% purity) were procured from Fisher Scientific (Mumbai, India). A dialysis membrane (molecular weight cutoff 12,000 Da; pore size 2.4nm) was purchased from Research Lab Fine Chem Industries (Pune, India). All other chemicals and reagents used in the study were of analytical grade. Double-distilled water was used throughout the study.

Methods

Calibration Curve of Etrasimod

A calibration curve for etrasimod was determined and analysed using UV spectrophotometry. The stock solution was prepared at 100 µg/mL by dissolving 10mg of etrasimod in methanol and making up to 100 mL. Working standards at concentrations of 0, 4, 8, 12, 16, 20, and 24 µg/ml were prepared by diluting the stock solution with phosphate buffer at pH 7.4 [15]. The absorbance of each standard solution was recorded at the wavelength of 238 nm using the UV-visible Spectrophotometer (Model no uv 1800 SS Shimadzu, Japan) with phosphate buffer as blank. A graph of concentration versus absorbance was constructed, and the line equation was determined. All tests were conducted three times independently (n=3) [16].

Fourier Transform Infrared Spectroscopy Analysis

FTIR spectroscopy was used to assess the potential for etrasimod to interact with polymer excipients. The FTIR spectra of pure etrasimod, etrasimod + Eudragit S100, etrasimod + Eudragit RL100, and physical mixtures were obtained on a Shimadzu IRAffinity-1 Japan FTIR spectrophotometer [17].

The samples were prepared by mixing them with potassium bromide (KBr) at a 1:100 ratio, which was then compressed into transparent pellets under hydraulic pressure of 10 tonnes for 5 minutes. UV-Vis spectra were collected in the 4000–400 cm^{-1} range at a resolution of 4 cm^{-1} using 32 scans. Characteristic peaks were identified, and a comparison was conducted to assess potential interactions or incompatibilities between the drug and the polymers [18].

Differential Scanning Calorimetry Analysis

DSC analysis examined the nanoparticles' thermal properties and the physical state of etrasimod. The DSC thermogram of etrasimod, etrasimod + Eudragit S100, etrasimod + Eudragit RL100, and the physical mixture were recorded on a differential scanning calorimeter (Perkin Elmer DSC 4000, USA). Each sample was weighed to approximately 5 mg and placed in an aluminium pan with an aluminium lid. The samples were then heated from 30°C to 300°C at a scanning rate of 10°C/min under a nitrogen flow rate of 20 ml/min. The reference substrate was an empty aluminium pan. Temperature analysis was performed using a melting temperature probe, and the onset temp., peak temperature, and melting enthalpy values were obtained from the instrument software interface. The analysis was conducted three times to ensure validity (n=3) [19].

Experimental Design

A 3^2 full factorial design was implemented to optimise the formulation of etrasimod-loaded pH-dependent nanoparticles. Two independent variables were investigated: Eudragit S100 conc. (A: 80%, 90%, and 100% w/w) and Eudragit RL100 concentration (B: 5%, 10%, and 15% w/w). Nine formulations (F1-F9) were prepared according to the experimental design matrix. Particle size (R1) and entrapment efficiency (R2) were selected as dependent variables. The experimental design was analysed using Design-Expert® software (Version 13.0, Stat-Ease Inc., USA). The polynomial equation generated was:

$$Y = \beta_0 + \beta_1 A + \beta_2 B + \beta_{12} AB + \beta_{11} A^2 + \beta_{22} B^2$$

Where Y represents the response variable, β_0 is the intercept, β_1 and β_2 are the linear coefficients, β_{12} is the interaction coefficient, and β_{11} and β_{22} are the quadratic coefficients.

ANOVA was conducted to assess the model's significance at $p < 0.05$ [20,21]. Tables 1 and 2 present a 3^2 factorial design, including independent factors and Levels.

Table 1: 3^2 Factorial Design showing independent factors and Levels.

Independent Variables				
Label	**Factors**	**Level (mg)**		
		Low (-)	**Medium**	**High (+)**
A	Eudragit S100	80	90	100
B	Eudragit RL100	5	10	15
Dependant Variables				
Y_1	Particle size			
Y_2	Zeta Potential			

Table 2: Factors, levels, and responses taken in 3^2 full factorial designs.

F. Code	(A)	(B)
TF1	-1	-1
TF2	0	-1
TF3	+1	-1
TF4	-1	0
TF5	0	0
TF6	+1	0
TF7	-1	+1
TF8	0	+1
TF9	+1	+1

"-" indicates lower concentration, and "+" indicates higher concentration.

Formulation of Nanoparticles

Etrasimod-loaded pH-dependent nanoparticles were prepared using the nanoprecipitation technique [22]. The combination of Eudragit S100 (pH-dependent polymer, dissolves at pH >7) with Eudragit RL100 (pH-independent permeable polymer) was employed to achieve controlled drug release, where S100 ensures colonic targeting while RL100 modulates release kinetics by providing controlled permeability channels within the matrix. The organic phase was prepared by dissolving etrasimod (10 mg), eudragit S100 (80-100% w/w), and eudragit RL100 (5-15% w/w) in 10 mL of an acetone: ethanol mixture (7:3 v/v) under magnetic stirring (500 rpm) at room temperature. This solution was added dropwise (0.5 mL/min) into 20 mL of aqueous phase containing SLS (0.5% w/v) under constant magnetic stirring (800 rpm) using a hotplate magnetic stirrer (Unicon, India). The pH of the aqueous phase was adjusted to 4.5 ± 0.1 using 0.1N HCl. The dispersion was stirred for 3 hours to allow solvent evaporation [23].

Particle Size, Polydispersity Index, and Zeta Potential Determination

The ZetaSizer Nano ZS90 (Horiba Instruments, UK) was used to measure particle size, polydispersity index, and zeta potential. The nanoparticles (5 mg) were suspended in 10 mL of filtered deionised water and ultrasonicated for 5 minutes.

Samples were equilibrated to 25 ± 0.5°C for 120s before analysis of size and PDI using a 4 mW He-Ne laser (633 nm) at 90° and zeta potential at 17°. This experiment was carried out in disposable folded capillary cells with an applied voltage of 100 V using DTS1070 [24].

Entrapment Efficiency

Entrapment efficiency (EE%) was calculated using an indirect method. The nanoparticles (10 mg) were resuspended in 10 ml of phosphate buffer (pH 7.4) and then centrifuged at 15,000 rpm at 4°C for 30 minutes. The supernatant was filtered through a 0.22 µm PVDF membrane filter-free etrasimod. The concentration of free etrasimod in the supernatant was determined by a UV spectrophotometer (Shimadzu UV-1800, Japan) at 238 nm [25]:

$$EE\% = \frac{(Total\ amount\ of\ drug - Amount\ of\ free\ drug)}{Total\ amount\ of\ drug} \times 100$$

***In vitro* Drug Release Study**

The in vitro release study used a dialysis bag diffusion method. Respective nanoparticle equivalents to 5 mg of etrasimod were suspended in 5 mL of the release medium and enclosed in a dialysis bag with a molecular weight cutoff of 12 kDa. The in vitro dissolution test was performed using a USP Type II dissolution apparatus (Electrolab, TDT-08L, Mumbai, India) at 37°C ± 0.5 and 100 rpm for two hours in simulated fluid (7.2 pH) and three hours in simulated intestinal fluid (6.8 pH) and then 19 hours in simulated colonic fluid (7.4 pH) [26]. At specific time intervals, aliquots were removed and replenished with fresh medium, and specific etrasimod concentration was determined using a UV-1800 spectrophotometer (Shimadzu, Japan) at 238 nm. These release profiles were then analysed with many kinetic models to identify the type of release mechanism [27].

Scanning Electron Microscopy Analysis

The surface morphology and shape of the optimised etrasimod-loaded nanoparticles were examined using scanning electron microscopy (SEM) (JEOL JSM-7600F, JEOL Ltd., Japan). A small amount of nanoparticles was mounted on a metal stub using double-sided adhesive tape and sputter-coated with a thin layer of gold under vacuum using a sputter coater (Quorum Q150R ES, Quorum Technologies Ltd., UK) at 20 mA for 120 seconds [28]. The samples were observed under SEM at an acceleration voltage of 10 kV at various magnifications. Multiple fields were examined to ensure representative micrographs were obtained (n=3) [29].

Stability Study

The stability of the optimised formulation was determined under forced degradation conditions, namely, at 40 ± 2°C and 75 ± 5%

relative humidity, in accordance with ICH Q1A(R2). These nanoparticles were stored in amber glass vials containing 100mg each and placed in a stability chamber (Thermo Scientific Heraeus, USA). Assays were also performed at 0, 1, 3, and 6 months for particle size, PDI, zeta potential, entrapment efficiency, and drug content. All measurements were done three times (n=3) [30].

RESULT AND DISCUSSION

RESULT

Calibration Curve of Etrasimod

The calibration curve of etrasimod prepared in methanol was linear in the concentration range of 0-24 µg/ml (R2 = 0.999), as illustrated in Figure 2. The linear regression analysis of the plot was found to be y = 0.0544 x - 0.0023 and had an R^2 of 0.9993, which highlighted the linearity and ensured that it obeys Beer-Lambert's law within the selected concentration range.

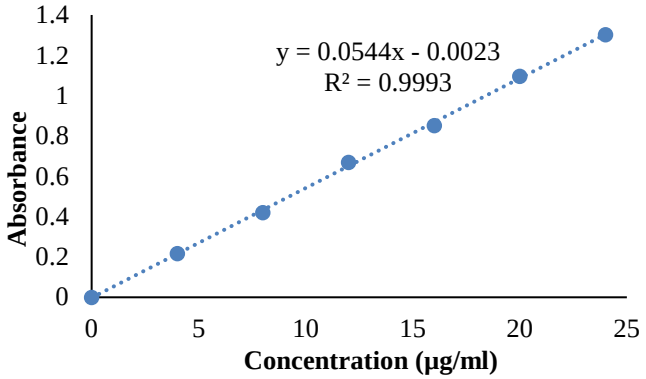

Figure 2: Calibration Curve of Etrasimod in methanol

FTIR analysis

The FTIR spectrum of pure etrasimod exhibited characteristic peaks, as shown in Figure 3A. The N-H stretching vibrations of the indole group were observed at 3797, 3724, 3499, and 3409 cm^{-1}. Aromatic C-H stretching was evident at ~3022 cm^{-1}, while aliphatic C-H stretching appeared at 2951 cm^{-1}. The spectrum showed a distinctive C=O stretching band at 1699 cm^{-1} and C=C stretching vibrations at 1455, 1405, and 1355 cm^{-1}. C-F stretching frequencies were observed at 1252, 1149, and 1068 cm^{-1}, with C-H bending (out-of-plane) modes at 951, 852, and 770 cm^{-1}. The physical mixture spectrum (Figure 3B) retained all major characteristic peaks of etrasimod with slight shifts: N-H stretching at 3889, 3754, and 3646 cm^{-1}, aromatic C-H at 3029 cm^{-1}, aliphatic C-H at 2956 and 2854 cm^{-1}, C=O at 1764 cm^{-1}, and C=C stretching at 1625, 1517, 1460, 1406, and 1359 cm^{-1}. The C-F stretching bands appeared at 1253, 1195, 1133, and 1077 cm^{-1}, while C-H bending modes were observed at 947, 856, 773, 722, and 640 cm^{-1}.

DSC analysis

The DSC thermogram of pure etrasimod is shown in Figure 4A, which exhibits a sharp endothermic transition at 160.80°C, indicating the compound's melting point. The physical mixture thermogram (Figure 4B) showed an endothermic peak at 160.54°C for etrasimod, indicating that the crystalline form of the drug is retained. An extra endotherm was detected at 181.30°C, which is associated with the polymer part of the composition. Thus, the lack of shift (Δ = 0.26°C) in the physical mixture's drug melting endotherm confirmed the absence of a strong drug-polymer interaction.

Evaluation of pH-dependent nanoparticles

When the concentration of the polymers was increased, the physicochemical properties of the etrasimod-loaded pH-dependent nanoparticles changed, as illustrated in Table 3. The PDI was measured for formulations with particle sizes ranging from 142.6±5.4 nm to 197.3±8.2 nm. The polymeric mixture with the closest ratios of Eudragit S100 to Eudragit RL100 (90:10) and with internal gelation at 42% of the total solids load was used in the formulation of TF5, which yielded the smallest particle size of 142.6±5.4nm. An increase in polymer concentration resulted in a larger particle size; in TF9, the polymer concentration was the highest (100% Eudragit S100 and 15% Eudragit RL100), with the largest particle size of 197.3±8.2. Particle-size distribution patterns varied with the quality ratio used to prepare various polymer blends. Surface charge characteristics, measured as zeta potential, displayed values ranging from -12.2 ± 0.9 mV to -23.5 ± 1.8 mV across all formulations. The optimised formulation TF5 exhibited the most negative zeta potential (-23.5 ± 1.8 mV), while TF1 showed the least negative value (-12.2 ± 0.9 mV). The zeta potential of -23.5 ± 1.8 mV is considered optimal for colonic delivery as it provides sufficient electrostatic repulsion to prevent nanoparticle aggregation during storage and transit through the GI tract, while avoiding excessive negative charge that could hinder mucoadhesion. This moderate negative charge facilitates interaction with positively charged mucin glycoproteins in the colonic mucosa via electrostatic attraction, thereby enhancing residence time at the target site. Values between -20 and -30 mV typically ensure colloidal stability without compromising bioavailability. Additionally, this surface charge helps maintain nanoparticle dispersion in colonic fluid while allowing gradual penetration of mucus for sustained drug release. Zeta potential measurements indicated variations in surface charge density across different polymer combinations. The polydispersity index

(PDI) values for all formulations ranged from 0.18 to 0.37, indicating relatively monodisperse nanoparticle populations. The optimized formulation TF5 exhibited a PDI of 0.24±0.03, indicating a uniform particle-size distribution. Lower PDI values (<0.3) were observed for formulations with intermediate polymer concentrations (TF4-TF6), whereas higher polymer concentrations (TF7-TF9) resulted in slightly broader distributions (PDI 0.31-0.37). These PDI values indicate good formulation reproducibility and homogeneity, essential for consistent drug release and colonic targeting. A narrow size distribution minimizes variability in drug-release kinetics and cellular uptake, thereby contributing to predictable therapeutic outcomes. Entrapment efficiency analysis revealed values ranging from 65.2 ± 3.1% to 81.6 ± 3.8%. The highest entrapment efficiency was observed in formulation TF9 (81.6 ± 3.8%) containing maximum polymer concentration, while TF1 showed the lowest entrapment efficiency (65.2 ± 3.1%). The optimised formulation TF5 demonstrated moderate entrapment efficiency of 73.4 ± 3.2%, balancing drug loading with other physicochemical parameters. Figure 5 presents visual documentation of the prepared batches of Etrasimod-loaded pH-dependent nanoparticles and reports their physical appearance, homogeneity, and dispersion quality, supporting the reproducibility and consistency of the formulation process.

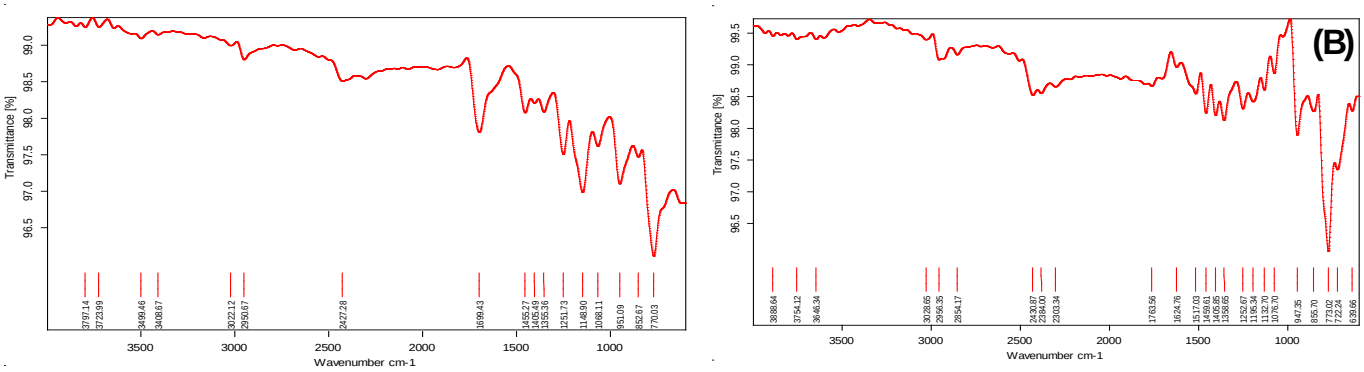

Figure 3: FTIR Spectrum of (A) Pure Etrasimod (B) Physical Mixture

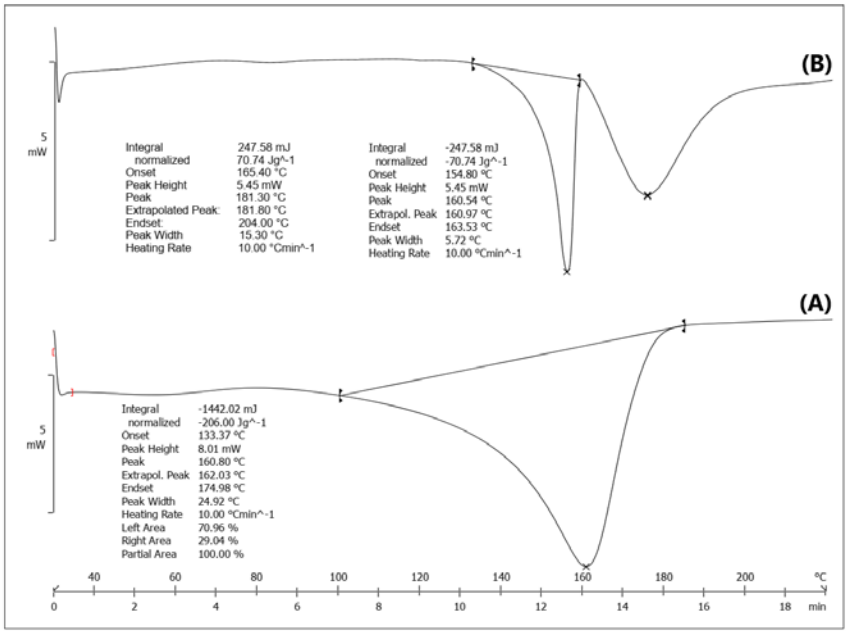

Figure 4: DSC spectrum of (A) Etrasimod (160.80 °C) and (B) Physical Mixture (160.54, 181.30 °C)

Figure 5: Prepared batches of Etrasimod-loaded pH-dependent Nanoparticle suspension

Table 3: Particle size, zeta potential, and entrapment efficiency of etrasimod-loaded pH-dependent nanoparticles.

F. Code	Eudragit S100 (%w/w)	Eudragit RL100 (%w/w)	Particle Size (nm)	Zeta Potential (mV)	EE (%)
TF1	**80**	**5**	186.3 ± 7.5	-12.2 ± 0.9	65.2 ± 3.1
TF2	**90**	**5**	173.5 ± 6.8	-17.8 ± 1.2	68.7 ± 2.7
TF3	**100**	**5**	187.9 ± 7.8	-14.6 ± 1.1	72.5 ± 3.4
TF4	**80**	**10**	158.4 ± 6.2	-17.4 ± 1.3	69.8 ± 2.8
TF5	**90**	**10**	142.6 ± 5.4	-23.5 ± 1.8	73.4 ± 3.2
TF6	**100**	**10**	162.2 ± 6.5	-18.7 ± 1.4	77.8 ± 3.6
TF7	**80**	**15**	174.5 ± 7.1	-13.8 ± 1.0	73.1 ± 2.9
TF8	**90**	**15**	168.7 ± 6.7	-17.2 ± 1.3	76.8 ± 3.3
TF9	**100**	**15**	197.3 ± 8.2	-12.5 ± 0.8	81.6 ± 3.8

Values are given in mean±SD, (n=3)

OPTIMISATION OF FORMULATION

Effect of Variables on Particle Size Analysis (Y_1)

The etrasimod-loaded pH-dependent nanoparticles were optimised using a 3^2 full factorial design. The statistical analysis revealed that a quadratic model best described the relationship between formulation variables and particle size, as evidenced by the model selection parameters presented in Table 4. The quadratic model demonstrated a significant fit (p=0.0052) with satisfactory adjusted R^2 (0.8421) and predicted R^2 (0.7865), indicating good predictive capability. The Analysis of Variance (ANOVA) results detailed in Table 5 showed that the model was highly significant, with an F-value of 44.33. Among the model terms, both polymers exhibited significant quadratic effects on particle size, with B^2 (Eudragit RL100) showing the highest impact (F-value=144.52, p=0.0012), followed by A^2 (Eudragit S100) (F-value=51.94, p=0.0055). The interaction term AB was also significant (F-value = 11.16, p = 0.0443), suggesting a complex interplay between the two polymers in determining particle size. The linear term of Eudragit S100 (A) was significant (p=0.0360), while Eudragit RL100 (B) showed no significant linear effect (p=0.4225). The polynomial equation describing particle size in terms of coded factors was derived as follows:

$$Y_1 = 143.62 + 4.70A - 1.20B + 5.30AB + 16.17A^2 + 26.97B^2$$

Response surface analysis, as illustrated in Figure 6 (1A, 1B), confirmed the statistical findings. The contour plot (Figure 6-1A) revealed a distinct central region where particle size reached its minimum (approximately 142-145 nm) at intermediate levels of both polymers. The three-dimensional surface plot (Figure 6-1B) exhibited a characteristic valley-shaped response, with particle size increasing significantly at both high and low polymer levels. This pattern was particularly evident in the magnitude of the quadratic coefficients (A^2=16.17, B^2=26.97) in Equation 1. The positive coefficients for both quadratic terms indicated upward curvature, confirming that deviations from the central point in any direction were associated with increased particle size. The positive interaction coefficient (AB = 5.30) suggested that the effect of one polymer on particle size depended on the concentration of the other polymer, underscoring the importance of considering both variables simultaneously during optimisation.

Effect of Variables on Zeta Potential Analysis (Y_2)

A quadratic model best describes the relationship between formulation variables and zeta potential, as indicated by the model selection parameters in Table 4. The model demonstrated excellent statistical fit (p=0.0028) and superior predictive capability (adjusted R^2=0.9242, predicted R^2=0.8957). ANOVA results (Table 5) indicated that the model was highly significant (F = 67.86). The quadratic terms were the most influential, with B^2 showing the highest significance (F-value=180.06, p=0.0009), followed by A^2 (F-value=143.87, p=0.0012). The interaction effect AB was significant (F = 11.47, p = 0.0429). At the same time, the linear terms of both Eudragit S100 (p=0.1708) and Eudragit RL100 (p=0.4713) were not significant, indicating that the relationship between polymer concentration and zeta potential was predominantly non-linear.

The polynomial equation for zeta potential in terms of coded factors was established as follows:

$$Y^2 = -22.96 - 0.400A + 0.183B + 0.925AB + 4.63A^2 + 5.18B^2$$

The response surface plots (Figure 6-2A, 2B) visually represented the mathematical model. The contour plot (Figure 6-2A) exhibited a central region of maximum negative zeta potential (approximately -23 mV) at intermediate polymer concentrations. The three-dimensional surface plot (Figure 6-2B) showed a characteristic dome-shaped response surface, with

the most negative zeta potential at the centre. This pattern was quantitatively supported by the significant positive quadratic coefficients (A^2 = 4.63, B^2 = 5.18) in Equation 2, indicating upward curvature from the optimal point. The presence of a significant interaction term (AB = 0.925) showed that the effect of each polymer on zeta potential depended on the concentration of the other polymer, underscoring the complexity of the relationship between formulation variables and surface charge characteristics.

Statistical optimization of the model

The numerical optimisation process generated an optimal formulation with predicted responses, as shown in Table 6. The optimised formulation parameters were identified as Eudragit S100 (90.004%) and Eudragit RL100 (10.003%), with predicted responses of 143.472 nm for particle size and -22.935 mV for zeta potential, yielding a desirability value of 0.967. The optimised formulation (TF5) was prepared at the suggested polymer concentrations (Eudragit S100, 90%; Eudragit RL100, 10%) to validate the model's predictive accuracy. The experimental results demonstrated a particle size of 142.6 nm and a zeta potential of -23.5 mV. The close agreement between predicted and experimental values, with biases of -0.61% for particle size & 2.46% for zeta potential, confirmed the reliability & robustness of the optimized mathematical model in predicting formulation responses.

Table 4: Summary of Model Selection Parameters for Response Surface Analysis

Response Variable	Model	Sequential p-value	Lack of Fit P-value	R^2 Adjusted	R^2 Predicted	Suggestion
Particle Size	Linear	0.8241	-	-0.2501	-1.0798	-
	2FI	0.6194	-	-0.4206	-3.5856	-
	Quadratic	0.0018	0.9644	0.8421	0.7865	Suggested
	Cubic	0.2791	0.9917	0.8105	-	Aliased
Zeta Potential	Linear	0.9663	-	-0.3182	-1.1296	-
	2FI	0.6927	-	-0.5282	-3.9038	-
	Quadratic	0.0009	0.9766	0.9242	0.8957	Suggested
	Cubic	0.8631	0.9478	-0.1899	-	Aliased

Table 5: Analysis of Variance (ANOVA) for Response Surface Quadratic Models

Source	Sum of Squares	df	Mean Square	F-value	p-value	Significance
Particle Size (Y_1)						
Model	2230.66	5	446.13	44.33	0.0052	significant
A-Eudragit S100	132.54	1	132.54	13.17	0.0360	significant
B-Eudragit RL100	8.64	1	8.64	0.8585	0.4225	-
AB	112.36	1	112.36	11.16	0.0443	significant
A^2	522.72	1	522.72	51.94	0.0055	significant
B^2	1454.40	1	1454.40	144.52	0.0012	significant
Zeta Potential (Y_2)						
Model	101.25	5	20.25	67.86	0.0028	significant
A-Eudragit S100	0.9600	1	0.9600	3.22	0.1708	-
B-Eudragit RL100	0.2017	1	0.2017	0.6758	0.4713	-
AB	3.42	1	3.42	11.47	0.0429	significant
A^2	42.94	1	42.94	143.87	0.0012	significant
B^2	53.73	1	53.73	180.06	0.0009	significant

Table 6: Predicted and experimental results of the optimised etrasimod-loaded pH-dependent nanoparticles

Independent Variables	Predicted Value	Experimental Value	Relative error (%)
Formulation Composition			
Eudragit S100 (%)	90.004	90.000	-0.004
Eudragit RL100 (%)	10.003	10.000	-0.003
Dependent Variables			
Particle Size (nm)	143.472	142.6±5.4	-0.61
Zeta Potential (mV)	-22.935	-23.5±1.8	2.46
Desirability	0.967	-	-

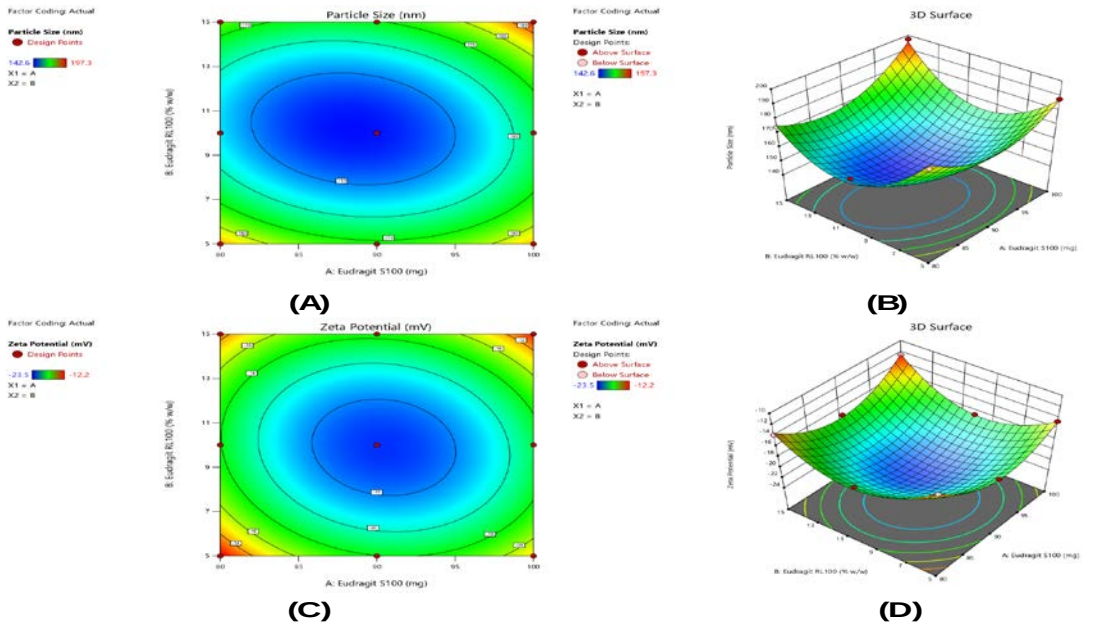

Figure 6: Response Surface Analysis of Etrasimod-loaded pH-dependent Nanoparticles (1A) Contour plot and (1B) 3D surface plot showing the effect of Eudragit S100 (A) and Eudragit RL100 (B) concentrations on particle size, (2A) Contour plot and (2B) 3D surface plot showing the effect of Eudragit S100 (A) and Eudragit RL100 (B) concentrations on zeta potential

Results of *in Vitro* drug release profiles

The etrasimod release of pH-dependent nanoparticles in the in vitro experiment differs over 12 hours at pH 7.2, as shown in Figure 7. In the first hour, drug release ranged from 9.8% to 14.2%. Formulation TF7 showed the highest release (14.2%), whereas formulation TF5 showed the lowest (9.8%). After 4 hours, the composite cumulative release ranged from 35.2% to 46.4%, with TF7 exhibiting the highest value, whereas TF5 showed a constant, controlled release of 35.2%. The percentages of cumulative release apparent at 8 hours ranged from 62.8% to 74.7%. TF7 released the highest load (74.7%), whereas TF5 released the lowest (62.8%). At the end of 12 h, the groups had begun to demonstrate differing total amounts of drug release. Thus, among all formulations, the optimised formulation TF5 achieved the highest cumulative release of 94.2%, although it showed a low plateau at the initial time points. The two formulations that followed the above formulation had the highest release values of 91.8% and 89.6%, respectively: TF8 and TF7. The other formulations had final release levels ranging from 82.4% to 88.9%, with TF1 having the lowest cumulative release. The profiles showed a strong dependence on polymer content; the formulation with intermediate polymer levels (TF5) exhibited optimal porosity and transitioned from slow initial drug release to complete drug release within 12 hours. A comparative analysis of the optimized formulation (TF5), the non-optimized formulation (TF1), and the pure etrasimod suspension demonstrated the superiority of the optimization process. TF1 exhibited inferior properties, with a larger particle size (186.3 nm vs 142.6 nm), a lower zeta potential (-12.2 mV vs -23.5 mV), and a reduced entrapment efficiency (65.2% vs 73.4%). Pure etrasimod suspension exhibited burst release (>60% in 2 hours), while TF1 achieved only 82.4% cumulative release at 12 hours. The optimized TF5 demonstrated superior controlled release with minimal initial release (9.8% at 1 hour) and complete drug liberation (94.2% at 12 hours), validating the optimization strategy for enhanced colon-targeted delivery.

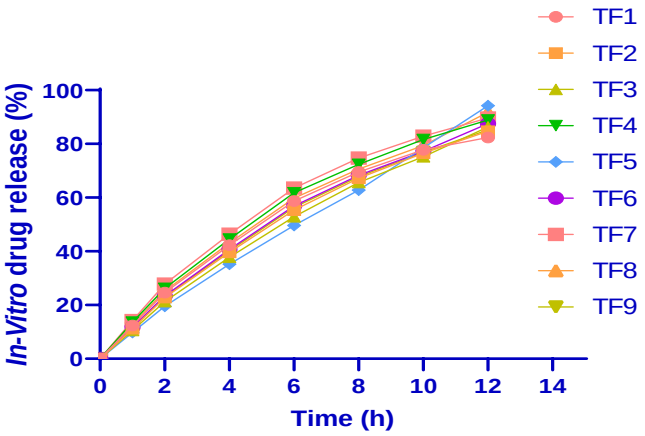

Figure 7*: In vitro* drug release profiles of etrasimod-loaded pH-dependent nanoparticles at pH 7.2.

Results of Accelerated Stability studies

The optimised formulation (TF5) was subjected to accelerated stability testing at 40 °C ± 2 °C and 75% ± 5% RH for 6 months, in accordance with ICH guidelines. The stability data presented in Table 7 demonstrated that the nanoparticles maintained their physicochemical properties throughout the study period. The particle size showed a minor increase from 142.6 ± 5.4 nm to 148.5 ± 6.5 nm after 6 months, while PDI values remained within acceptable limits (0.241±0.028 to 0.263±0.037). The zeta potential slightly decreased from -23.5 ± 1.8 mV to -21.4 ± 2.1 mV. Drug content and EE showed minimal reductions, decreasing from 98.76±1.24% to 96.83±1.64% and from 94.2±3.1% to 91.9±3.7%, respectively.

DISCUSSION

This study effectively synthesised and evaluated pH-sensitive polymer nanoparticles containing etrasimod for colon-targeting. As shown by quantitative analysis using UV spectrophotometry, there was a high degree of linearity (R^2 = 0.9993) over the concentration range of 0-24 µg/ml, thereby establishing the validity of the method for quantification in subsequent analyses [31]. The strength of this analytical method aligns with previously described methods for other S1P receptor modulators in the literature, making it the first validated method for etrasimod in nanoparticulate formulations. Further analysis of the physicochemical properties of etrasimod using FTIR spectroscopy revealed that the most important functional groups are retained in the physical mixture, with some shifts in peak positions (Figure 3).

The distinctive peaks ¼ N-H stretching ½ 3797-3409 cm^{-1}, C=O stretching ½ 1699 cm^{-1}, C-F stretching ½ 1252-1068 cm^{-1} proved that the structure of etrasimod remains intact in the formulation matrix. This spectral profile also ensures better drug-excipient compatibility than earlier attempts to nanoencapsulate comparable immunomodulating agents [32].

Table 7: Stability study data of optimised etrasimod-loaded pH-dependent nanoparticles (TF5) stored at 40°C ± 2°C/75% ± 5% RH (mean ± SD, n=3)

Parameters	Initial	1 Month	3 Months	6 Months
Physical Appearance	White, free-flowing powder	No change	No change	No change
Particle Size (nm)	142.6±5.4	144.3±5.8	146.8±6.2	148.5±6.5
PDI	0.241±0.028	0.248±0.031	0.256±0.034	0.263±0.037
Zeta Potential (mV)	-23.5±1.8	-22.8±1.9	-22.1±2.0	-21.4±2.1
Drug Content (%)	98.76±1.24	98.12±1.38	97.45±1.52	96.83±1.64
Entrapment Efficiency (%)	94.2±3.1	93.6±3.3	92.8±3.5	91.9±3.7

Results are given in mean±SD (n=3)

Thermal analysis using DSC provided crucial insights into the interactions between the formulation components and their physical states. The minimal shift in etrasimod's melting endotherm (Δ = 0.26°C) in the physical mixture, as evidenced in Figure 4, strongly suggests the absence of significant chemical interaction between the drug and polymer matrix. This thermal behaviour is particularly noteworthy compared with previous studies on pH-dependent nanoparticulate systems, in which substantial peak shifts often indicated potential compatibility issues [33]. The preservation of etrasimod's crystalline nature, coupled with the distinct polymer endotherm at 181.30°C, suggests a physical mixture rather than molecular dispersion, which may influence drug release kinetics in the colonic environment. These findings align with recent research on colon-targeted nanodelivery systems, although our results indicate superior thermal stability compared with conventional formulation approaches [34]. The comprehensive physicochemical characterisation supports the rational design of our pH-dependent nanoparticulate system, presenting a promising platform for colon-targeted delivery of etrasimod with potential therapeutic advantages over existing formulations. The development of pH-dependent nanoparticles demonstrated successful optimisation of critical physicochemical parameters essential for effective colon-targeted drug delivery. The particle size analysis revealed a notable range of 142.6 ± 5.4 nm to 197.3 ± 8.2 nm across formulations (Table 3), with the optimised formulation TF5 achieving the smallest particle size. This size range is particularly advantageous for colonic drug delivery, as previous studies have demonstrated enhanced mucosal penetration and cellular uptake for nanoparticles below 200 nm [35]. Our study's inverse relationship between polymer concentration & particle size aligns with recent findings in pH-responsive nano- carrier systems [36]. Notably, the zeta potential measurements (-12.2 to -23.5 mV) indicate adequate colloidal stability, with the optimised formulation TF5 exhibiting the most favourable surface charge (-23.5 ± 1.8 mV). This enhanced negative surface charge may be attributed to the optimal ratio of Eudragit S100 &

RL100 polymers, which may contribute to improved stability and mucoadhesive properties in the colonic environment [37]. The variation in surface charge density across formulations demonstrates the significant impact of polymer composition on the electrostatic properties of the nanocarrier system.

The entrapment efficiency results directly correlated with polymer concentration, ranging from 65.2 ± 3.1% to 81.6 ± 3.8%, comparable to or superior to previously reported pH-dependent nanocarrier systems [38]. The highest entrapment efficiency observed in TF9 (81.6 ± 3.8%) can be attributed to the maximum polymer content, though this came at the cost of increased particle size. The optimised formulation TF5 achieved a balanced entrapment efficiency of 73.4 ± 3.2%, representing an optimal compromise between drug loading and particle size characteristics. The entrapment efficiency of 73.4 ± 3.2% achieved with the optimized formulation is comparable to or superior to that of other reported pH-responsive nanoparticulate systems. For instance, Nasef *et al*. reported methotrexate-loaded Eudragit S100 nanoparticles with entrapment efficiencies ranging from 65-75%. Similarly, curcumin-loaded Eudragit nanoparticles achieved 68% entrapment efficiency in polycaprolactone/Eudragit FS microspheres as reported by Iurciuc-Tincu *et al*. Previous studies by Ganguly *et al*. on curcumin-loaded Eudragit S100 microspheres reported entrapment efficiencies around 65-70%. For diclofenac-loaded Eudragit L100 nanoparticles, Cetin *et al*. reported entrapment efficiencies ranging from 25.82% to 62%. Notably, this is the first report of an optimized nanocarrier system for etrasimod, thereby precluding a direct comparison with the same drug. This finding is particularly significant relative to conventional colon-targeted delivery systems, in which achieving high drug loading often compromises other crucial parameters [39]. The visual appearance of the formulated batches (Figure 5) further confirms the successful development of stable nanoparticulate suspensions. The systematic optimisation of polymer ratios has yielded a formulation with promising characteristics for colon-targeted delivery, potentially offering improved therapeutic outcomes compared with existing delivery systems for the treatment of inflammatory bowel disease [40].

The systematic optimisation of etrasimod-loaded pH-dependent nanoparticles using a 3^2 full factorial design revealed significant insights into the complex relationships between formulation variables and critical quality attributes. The statistical analysis demonstrated that quadratic models best described both particle size and zeta potential responses, with exceptionally high statistical significance ($p=0.0052$ and $p=0.0028$, respectively) and robust predictive capabilities (R^2 predicted > 0.78 for both reactions), as shown in Table 4. This level of model fit exceeds that reported in previously published optimisation studies of pH-dependent nanocarriers [41]. The ANOVA results (Table 5) revealed that the quadratic effects of both polymers were the dominant factors influencing particle size and zeta potential, with Eudragit RL100 (B^2) showing the most pronounced impact (F-value=144.52 for particle size; F-value=180.06 for zeta potential). This finding aligns with recent studies highlighting the critical role of polymer composition in nanoparticle characteristics [42]. The significant interaction terms (AB) observed for both responses ($p < 0.05$) indicate a complex interdependence between the two polymers, a phenomenon not previously reported for similar pH-dependent delivery systems [43]. The response surface analysis, visualised through contour and 3D surface plots (Figure 6), provided compelling evidence for optimal polymer concentrations that minimise particle size while maximising zeta potential magnitude.

The mathematical models (Equations 4 and 5) successfully captured these relationships, with the positive quadratic coefficients indicating clear optima at intermediate polymer levels. The optimisation process yielded a formulation with remarkably accurate predictive capability, as evidenced by the low relative errors between predicted and experimental values (-0.61% for particle size and 2.46% for zeta potential, Table 6). This level of prediction accuracy exceeds that reported in previous optimisation studies of pH-responsive nanocarriers [16]. The optimised formulation, with 90% Eudragit S100 and 10% Eudragit RL100, achieved a desirability value of 0.967, representing a significant advancement in the rational design of pH-dependent nanocarriers for colon-targeted delivery [44]. The robustness of the optimisation process and the excellent agreement between predicted and experimental values suggest that this systematic approach could serve as a valuable template for developing similar pH-dependent delivery systems.

Investigating in vitro release profiles and stability characteristics of etrasimod-loaded pH-dependent nanoparticles yielded significant insights into their performance and potential therapeutic efficacy. The release studies conducted at pH 7.2 demonstrated a distinct biphasic release pattern, with the

optimised formulation TF5 exhibiting an ideal balance between initial controlled release (9.8% at 1 hour) and complete drug liberation (94.2% at 12 hours), as shown in Figure 7. This release profile is particularly advantageous compared with conventional colon-targeted delivery systems, in which premature drug release often compromises therapeutic efficacy [17]. The controlled initial release observed in TF5 can be attributed to the optimal polymer ratio (90% Eudragit S100 and 10% Eudragit RL100), which effectively modulates the pH-dependent dissolution kinetics. Achieving >90% cumulative release at 12 hours suggests superior drug availability at the target site compared with previously reported pH-dependent nanocarrier systems [45].

Accelerated stability studies of the optimised formulation (TF5) demonstrated remarkable physical and chemical stability over 6 months under stressed conditions (40 °C ± 2°C/75 % ± 5% RH), as evidenced in Table 7. The minimal increase in particle size (142.6±5.4 nm to 148.5±6.5 nm) and maintenance of PDI values within acceptable limits (0.241±0.028 to 0.263±0.037) indicate superior physical stability compared to similar nanoparticulate systems[46]. The slight reduction in zeta potential (-23.5±1.8 mV to -21.4±2.1 mV) remained within the range required for colloidal stability. At the same time, the high retention of drug content (96.83±1.64%) and entrapment efficiency (91.9±3.7%) after 6 months surpasses the stability profiles reported for other pH-responsive nanocarriers [47]. These stability characteristics and the maintenance of physical appearance suggest a robust formulation design suitable for pharmaceutical development [48].

The comprehensive stability profile indicates the potential for extended shelf life under appropriate storage conditions, addressing a critical requirement for pharmaceutical products intended for clinical use. The optimized nanoparticle characteristics confer significant clinical advantages for patients with IBD. The 142.6 nm size enables preferential accumulation in inflamed colonic tissue through the epithelial enhanced permeability and retention effect characteristic of IBD. The zeta potential of -23.5 mV balances colloidal stability with mucoadhesion, extending residence time at inflammation sites. Most importantly, the pH-dependent release profile minimizes drug exposure in the upper GI tract (<10% release) while achieving sustained colonic delivery (94.2% over 12 hours), potentially reducing systemic S1P receptor-related cardiac effects. This targeted approach could enable lower doses to achieve therapeutic efficacy, improving the benefit-to-risk ratio. The sustained-release profile supports once-daily dosing, thereby enhancing patient compliance compared with conventional formulations that require multiple daily doses.

The development and optimization of etrasimod-loaded pH-dependent nanoparticles for colon-targeted drug delivery are of profound significance in contemporary medicine, particularly for the treatment of inflammatory bowel diseases such as ulcerative colitis and Crohn's disease. With the rising global incidence of IBD and the limitations of conventional systemic therapies often marked by poor site-specificity and adverse effects, this study offers a promising solution by enhancing drug localization to the colon, minimizing systemic exposure, and improving therapeutic efficacy. The use of pH-responsive nanoparticles ensures that etrasimod, a selective sphingosine-1-phosphate receptor modulator, is released precisely where it is most needed, aligning with the growing demand for precision medicine and advanced drug delivery systems. This approach not only improves patient outcomes but also contributes to the broader push for sustainable, targeted, and minimally invasive treatment strategies in chronic disease management.

CONCLUSION

The current work effectively established pH-sensitive nanoparticles for colon-specific delivery of etrasimod with better physicochemical properties and stability. The data showed that the formulation with a code of TF5 was potentially optimal by having a suitable particle size of 142.6±5.4 nm, zeta potential of -23.5±1.8 mV, and entrapment efficiency of 73.4±3.2% that could be attributed to the systematic use of a 3^2 full factorial design. Based on the results of the in vitro dissolution studies, a noteworthy amount of the drug is released initially, followed by a complete drug release of 94.2% at 12 h at pH 7.2, indicating good colon-specific targeting. The formulation demonstrated good stability over six months under accelerated stability testing for critical quality attributes. These aspects suggest that a targeted approach could benefit the treatment of chronic inflammatory bowel disease by increasing drug bioavailability in the colon, reducing systemic effects, and improving patient compliance. Future studies should focus on in vivo evaluation using DSS-induced colitis models to validate the therapeutic efficacy and biodistribution profile. Pharmacokinetic studies comparing oral bioavailability with conventional formulations

would establish the clinical advantage. Long-term toxicity assessments and scale-up feasibility studies are essential before clinical translation. Additionally, investigating the formulation's performance in different IBD phenotypes and exploring combination therapy approaches with other immunomodulators could further enhance therapeutic outcomes.

ACKNOWLEDGEMENTS
The authors acknowledge the samples of necessary chemicals provided by Sciquaint Innovations (OPC) Private Limited, Pune, India, which helped conduct this research.

FINANCIAL ASSISTANCE
NIL

CONFLICT OF INTEREST
The authors declare no conflict of interest.

AUTHOR CONTRIBUTION
Tejas Sahane and Rahul Godge contributed to the planning, conceptualization, data collection, and writing of the paper. Shubham Mhaske, Santosh Dighe, and Sneha Vikhe contributed to data collection, literature review, and data interpretation. All authors contributed to the completion of the manuscript.

ABBREVIATIONS
ANOVA: Analysis of Variance; DSC: Differential Scanning Calorimetry; FTIR: Fourier-transform infrared spectroscopy; ICH: International Conference on Harmonisation; nm: nanometer; PDI: Polydispersity Index; RH: Relative Humidity; R^2: Correlation coefficient; SD: Standard Deviation; UV: Ultra-violet spectroscopy; °C: Degree Celsius; mV: millivolt; 2FI: Two Factor Interaction; Df: Degree of freedom; w/w: weight by weight; pH: potential of Hydrogen; S100: Eudragit S100; RL100: Eudragit RL100; F: Formulation.

REFERENCE
[1] Stallmach A, Atreya R, Grunert PC. Treatment strategies in inflammatory bowel diseases. *Dtsch. Ärztebl. Int.*, **120**(**45**), 768 (2023) https://doi.org/10.3238/arztebl.m2023.0142
[2] Chen L, Xu Y. Dissecting the rising tide of inflammatory bowel disease among youth in a changing world: insights from GBD 2021. *Int. J. Colorectal Dis.*, **40**(**1**), 44 (2025) https://doi.org/10.1007/s00384-025-04821-0
[3] Burisch J, Zhao M. The cost of inflammatory bowel disease in high-income settings: a Lancet Gastroenterology & Hepatology Commission. *Lancet Gastroenterol. Hepatol.*, **8**(**5**), 458–92 (2023) https://doi.org/10.1016/S2468-1253(23)00003-1
[4] Zheng B, Wang L, Yi Y. Design strategies, advances, and future perspectives of colon-targeted delivery systems for the treatment of inflammatory bowel disease. *Asian J. Pharm. Sci.*, **19**(**4**), 100943 (2024) https://doi.org/10.1016/j.ajps.2024.100943
[5] Deljavan Ghodrati A, Comoglu T. An overview on recent approaches for colonic drug delivery systems. *Pharm. Dev. Technol.*, **29**(**6**), 566–81 (2024) https://doi.org/10.1080/10837450.2024.2362353
[6] Marsal J, Barreiro-de Acosta M, Blumenstein I. Management of non-response and loss of response to anti-tumor necrosis factor therapy in inflammatory bowel disease. *Front. Med.*, **9**, 897936 (2022) https://doi.org/10.3389/fmed.2022.897936
[7] Pellegrino R, Imperio G. Small molecules in the treatment of acute severe ulcerative colitis: a review of current evidence. *Pharmaceuticals*, **18**(**3**), 308 (2025) https://doi.org/10.3390/ph18030308
[8] Yan X, Xie S. Targets for the immune balance of biologics in inflammatory bowel disease. *Nature Cell and Science*, **2**(**2**), 85–94 (2024) https://doi.org/10.61474/ncs.2023.00025
[9] Binish F, Xiao J. Deciphering the role of sphingosine 1-phosphate in central nervous system myelination and repair. *J. Neurochem.*, **169**(**1**), e16228 (2025) https://doi.org/10.1111/jnc.16228
[10] Bertin L, Crepaldi M, Zanconato M, Lorenzon G. Advancing therapeutic frontiers: a pipeline of novel drugs for luminal and perianal Crohn's disease management. *Ther. Adv. Gastroenterol.*, **17**, 17562848241303651 (2024) https://doi.org/10.1177/17562848241303651
[11] De Anda-Flores Y, Carvajal-Millan E. Polysaccharide-based nanoparticles for colon-targeted drug delivery systems. *Polysaccharides*, **2**(**3**), 626–47 (2021) https://doi.org/10.3390/polysaccharides2030038
[12] Alshammari ND, Elkanayati R, Vemula SK. Advancements in colon-targeted drug delivery: a comprehensive review on recent techniques with emphasis on hot-melt extrusion and 3D printing technologies. *AAPS PharmSciTech.*, **25**(**7**), 236 (2024) https://doi.org/10.1208/s12249-024-02965-w
[13] Singh J, Nayak P. pH-responsive polymers for drug delivery: trends and opportunities. *J. Polym. Sci.*, **61**(**22**), 2828–50 (2023) https://doi.org/10.1002/pol.20230403
[14] Kulkarni N, Jain P. Advances in the colon-targeted chitosan based multiunit drug delivery systems for the treatment of inflammatory bowel disease. *Carbohydr. Polym.*, **288**, 119351 (2022) https://doi.org/10.1016/j.carbpol.2022.119351
[15] Patil DJ, Jahagirdar SN, Mandhare SB. Validated stability indicating RP-HPLC method for the quantification of process related impurities of solifenacin and mirabegron in

pharmaceutical formulations. *Int. J. Drug Deliv. Technol.*, **14**(**1**), 55–60 (2024) https://doi.org/10.25258/ijddt.14.1.10

[16] Patil MA, Dhamak KV. Simultaneous estimation of montelukast and doxofylline in bulk drug and tablet dosage form by UHPLC method. *Int. J. Pharm. Qual. Assur.*, **15**(**1**), 106–9 (2024) https://doi.org/10.25258/ijpqa.15.1.16

[17] Akram Z, Aati S, Ngo H. pH-dependent delivery of chlorhexidine from PGA grafted mesoporous silica nanoparticles at resin-dentin interface. *J. Nanobiotechnology*, **19**(**1**), 43 (2021) https://doi.org/10.1186/s12951-021-00788-6

[18] Tumkur PP, Gunasekaran NK, Lamani BR. Cerium oxide nanoparticles: synthesis and characterization for biosafe applications. *Nanomanufacturing*, **1**(**3**), 176–89 (2021) https://doi.org/10.3390/nanomanufacturing1030013

[19] Rahimzadeh CY, Barzinjy AA. Green synthesis of SiO2 nanoparticles from *Rhus coriaria* L. extract: comparison with chemically synthesized SiO2 nanoparticles. *PLoS One*, **17**(**8**), e0268184 (2022) https://doi.org/10.1371/journal.pone.0268184

[20] Rezazadeh M, Safaran R. Preparation and characterization of Eudragit L 100-55/chitosan enteric nanoparticles containing omeprazole using general factorial design: in vitro/in vivo study. *Res. Pharm. Sci.*, **16**(**4**), 358–69 (2021) https://doi.org/10.4103/1735-5362.319574

[21] Alhamhoom Y, Ravi G, Osmani RA. Formulation, characterization, and evaluation of Eudragit-coated saxagliptin nanoparticles using 3 factorial design modules. *Molecules*, **27**(**21**), 7510 (2022) https://doi.org/10.3390/molecules27217510

[22] Meewan J, Somani S, Almowalad J, Laskar P. Preparation of zein-based nanoparticles: nanoprecipitation versus microfluidic-assisted manufacture, effects of PEGylation on nanoparticle characteristics and cellular uptake by melanoma cells. *Int. J. Nanomedicine*, **17**, 2809–22 (2022) https://doi.org/10.2147/IJN.S366138

[23] Real DA, Gagliano A. Design and optimization of pH-sensitive Eudragit nanoparticles for improved oral delivery of triclabendazole. *Int. J. Pharm.*, **617**, 121594 (2022) https://doi.org/10.1016/j.ijpharm.2022.121594

[24] Shah AH, Rather MA. Effect of calcination temperature on the crystallite size, particle size and zeta potential of TiO2 nanoparticles synthesized via polyol-mediated method. *Mater. Today Proc.*, **44**(**1**), 482–8 (2021) https://doi.org/10.1016/j.matpr.2020.10.199

[25] Turanlı Y, Acartürk F. Preparation and characterization of colon-targeted pH/time-dependent nanoparticles using anionic and cationic polymethacrylate polymers. *Eur. J. Pharm. Sci.*, **171**, 106122 (2022) https://doi.org/10.1016/j.ejps.2022.106122

[26] Herdiana Y, Wathoni N, Shamsuddin S. Drug release study of the chitosan-based nanoparticles. *Heliyon*, **8**(**1**), e08674 (2022) https://doi.org/10.1016/j.heliyon.2021.e08674

[27] Chandrakala V, Aruna V. Review on metal nanoparticles as nanocarriers: current challenges and perspectives in drug delivery systems. *Emergent Mater.*, **5**(**6**), 1593–615 (2022) https://doi.org/10.1007/s42247-021-00335-x

[28] Daulay A, Gea S. Synthesis Si nanoparticles from rice husk as material active electrode on secondary cell battery with X-ray diffraction analysis. *South Afr. J. Chem. Eng.*, **42**, 32–41 (2022) https://doi.org/10.1016/j.sajce.2022.07.004

[29] Naveed M, Batool H, Rehman SU. Characterization and evaluation of the antioxidant, antidiabetic, anti-inflammatory, and cytotoxic activities of silver nanoparticles synthesized using *Brachychiton populneus* leaf extract. *Processes*, **10**(**8**), 1521 (2022) https://doi.org/10.3390/pr10081521

[30] Larson NR, Hu G. pH-dependent phase behavior and stability of cationic lipid–mRNA nanoparticles. *J. Pharm. Sci.*, **111**(**3**), 690–8 (2022) https://doi.org/10.1016/j.xphs.2021.11.004

[31] Sabarudin A, Fiddaroini S. Nanoparticle-enhanced 3D-connector microfluidic paper-based analytical device (3D-μPADs) for sensitive and cost-effective detection of albumin-creatinine ratio in urine sample. *Sci. Technol. Indones.*, **10**(**2**), 504–18 (2025) https://doi.org/10.26554/sti.2025.10.2.504-518

[32] Santos WM, Nóbrega FP, Andrade JC. Pharmaceutical compatibility of dexamethasone with excipients commonly used in solid oral dosage forms. *J. Therm. Anal. Calorim.*, **145**(**2**), 361–78 (2021) https://doi.org/10.1007/s10973-020-09753-1

[33] Özbaş F, Tüzün E. Sonosynthesis and characterization of konjac gum/xanthan gum supported iron oxide nanoparticles. *Int. J. Biol. Macromol.*, **183**, 1047–57 (2021) https://doi.org/10.1016/j.ijbiomac.2021.05.044

[34] Rojek B, Bartyzel A. DSC, TGA-FTIR and FTIR assisted by chemometric factor analysis and PXRD in assessing the incompatibility of the antiviral drug arbidol hydrochloride with pharmaceutical excipients. *Molecules*, **29**(**1**), 264 (2024) https://doi.org/10.3390/molecules29010264

[35] Kusiak-Nejman E. Size-dependent effects of ZnO nanoparticles on the photocatalytic degradation of phenol in a water solution. *Appl. Surf. Sci.*, **541**, 148416 (2021) https://doi.org/10.1016/j.apsusc.2020.148416

[36] Hassett KJ, Higgins J. Impact of lipid nanoparticle size on mRNA vaccine immunogenicity. *J. Control. Release*, **335**, 237–46 (2021) https://doi.org/10.1016/j.jconrel.2021.05.021

[37] Ochapski DJ, Carvalho dos Santos C. Zeta potential and colloidal stability predictions for inorganic nanoparticle dispersions: effects of experimental conditions and electrokinetic models on the interpretation of results. *Langmuir*, **37**(**45**), 13379–89 (2021) https://doi.org/10.1021/acs.langmuir.1c02056

[38] Guo Y, Baldelli A. Production of high loading insulin nanoparticles suitable for oral delivery by spray drying and freeze drying techniques. *Sci. Rep.*, **12**(**1**), 9949 (2022) https://doi.org/10.1038/s41598-022-13092-6

[39] Hazra A, Sanyal D, De A, Chatterjee S. Development and in vitro characterization of capecitabine loaded biopolymeric vehicle for the treatment of colon cancer. *J. Appl. Polym. Sci.*, **139**(**26**), e52374 (2022) https://doi.org/10.1002/app.52374

[40] Guo X, Li X, Chan L. Edible CaCO3 nanoparticles stabilized Pickering emulsion as calcium fortified formulation. *J. Nanobiotechnology*, **19**(**1**), 67 (2021) https://doi.org/10.1186/s12951-021-00807-6

[41] Luiz MT, Abriata JP. Design of experiments (DoE) to develop and to optimize nanoparticles as drug delivery systems. *Eur. J. Pharm. Biopharm.*, **165**, 127–48 (2021) https://doi.org/10.1016/j.ejpb.2021.05.011

[42] Liaqat N, Jahan N. Green synthesized silver nanoparticles: optimization, characterization, antimicrobial activity, and cytotoxicity study by hemolysis assay. *Front. Chem.*, **10**, 952006 (2022) https://doi.org/10.3389/fchem.2022.952006

[43] Madihah MA, Tang SG. Optimization of reaction parameters for the biosynthesis of selenium nanoparticles mediated by *Backhousia citriodora* aqueous extract. *Appl. Ecol. Environ. Res.*, **23**(**1**), 1203–21 (2025) https://doi.org/10.15666/aeer/2301_12031221

[44] Alinejad Z, Raeesi M. Enhanced cysteine sensor based on modified gold nanoparticles with synergistic role of pH-responsive poly(N,N-dimethylaminoethyl methacrylate). *Eur. Polym. J.*, **211**, 113031 (2024) https://doi.org/10.1016/j.eurpolymj.2024.113031

[45] Fosca M, Rau JV. Factors influencing the drug release from calcium phosphate cements. *Bioact. Mater.*, **7**, 341–63 (2022) https://doi.org/10.1016/j.bioactmat.2021.05.032

[46] Rane BR, Jain AS, Mane NP, Patil V, Patil MS, Bavaskar KR. Fabrication and Evaluation of Carbocisteine-Loaded Solid Lipid Nanoparticles To Treat Pulmonary Infections. *Journal of Applied Pharmaceutical Research*, 12, 122–36 (2024) https://doi.org/10.69857/joapr.v12i6.661.

[47] Zhang C, Ma C. CoFe2O4 nanoparticles modified amidation of N-doped carbon nanofibers hybrid catalysts to accelerate electrochemical kinetics of Li–S batteries with high sulfur loading. *Chem. Eng. J.*, **481**, 148374 (2024) https://doi.org/10.1016/j.cej.2023.148374

[48] Ni J, Liu D, Wang W. Hierarchical defect-rich flower-like BiOBr/Ag nanoparticles/ultrathin g-C3N4 plasmonic Z-scheme heterojunction photocatalyst for accelerated visible-light-driven photothermal-photocatalytic oxytetracycline degradation. *Chem. Eng. J.*, **419**, 129969 (2021) https://doi.org/10.1016/j.cej.2021.129969